

Development of Magnetocaloric Microstructures from Equiatomic Iron–Rhodium Nanoparticles through Laser Sintering

Shabbir Tahir, Joachim Landers, Soma Salamon, David Koch, Carlos Doñate-Buendía, Anna R. Ziefuß, Heiko Wende, and Bilal Gökce*

Pronounced magnetocaloric effects are typically observed in materials that often contain expensive and rare elements and are therefore costly to mass produce. However, they can rather be exploited on a small scale for miniaturized devices such as magnetic micro coolers, thermal sensors, and magnetic micropumps. Herein, a method is developed to generate magnetocaloric microstructures from an equiatomic iron–rhodium (FeRh) bulk target through a stepwise process. First, paramagnetic near-to-equiatomic solid-solution FeRh nanoparticles (NPs) are generated through picosecond (ps)-pulsed laser ablation in ethanol, which are then transformed into a printable ink and patterned using a continuous wave laser. Laser patterning not only leads to sintering of the NP ink but also triggers the phase transformation of the initial γ - to B2-FeRh. At a laser fluence of 246 J cm^{-2} , a partial (52%) phase transformation from γ - to B2-FeRh is obtained, resulting in a magnetization increase of $35 \text{ Am}^2 \text{ kg}^{-1}$ across the antiferromagnetic to ferromagnetic phase transition. This represents a ca. sixfold enhancement compared to previous furnace-annealed FeRh ink. Finally, herein, the ability is demonstrated to create FeRh 2D structures with different geometries using laser sintering of magnetocaloric inks, which offers advantages such as micrometric spatial resolution, in situ annealing, and structure design flexibility.


scaffolds.^[13–15] The performance and size of these devices rely on the capability to produce 2D miniaturized electronics-based and semiconductor-based devices.^[16–20] Advancements in this field and the diversity of printing techniques have facilitated device miniaturization, thereby allowing size reduction of common electronics such as laptops, smart watches, pocket calculators, and the development of minuscule sensors.^[21,22] Screen and nozzle printing techniques were employed to produce micron-size supercapacitors on paper, which can be used as a portable energy-storage device.^[23] Although the printing technique is fast, low cost, and highly efficient, the screen cleaning process is difficult and time-consuming.^[19] Photolithography was implemented to print micro-patterned electrode-based sensors on flexible substrates for glucose monitoring.^[24] However, the technique consists of many processing steps and requires a pre-designed photoresist layer, which can be difficult to produce. One of the most used

1. Introduction

Printing techniques using nanoparticle (NP) inks are utilized to generate thin films and structured materials with precise geometry. These methods are widely employed in the production of 2D structures, including solar cells,^[1–3] light-emitting diodes (LEDs),^[4–6] batteries,^[7–9] sensors,^[10–12] and biological

techniques to deposit NP inks on the desired substrate is inkjet printing. Grubb et al.^[20] have successfully achieved the inkjet printing of transistors with a channel size of $1 \mu\text{m}$, enabling its integration into a smaller footprint on a chip. For individual printed material layers, oven curing is often employed making the fabrication technique time-consuming. Additionally, inkjet printers often have issues with head reliability, droplet formation

S. Tahir, C. Doñate-Buendía, B. Gökce
Chair of Materials Science and Additive Manufacturing
University of Wuppertal
Gaußstr. 20, 42119 Wuppertal, Germany
E-mail: goekce@uni-wuppertal.de

 The ORCID identification number(s) for the author(s) of this article can be found under <https://doi.org/10.1002/adem.202300245>.

© 2023 The Authors. Advanced Engineering Materials published by Wiley-VCH GmbH. This is an open access article under the terms of the Creative Commons Attribution-NonCommercial License, which permits use, distribution and reproduction in any medium, provided the original work is properly cited and is not used for commercial purposes.

DOI: 10.1002/adem.202300245

J. Landers, S. Salamon, H. Wende
Faculty of Physics and Center for Nanointegration Duisburg-Essen
(CENIDE)
University of Duisburg-Essen
Lotharstr. 1, 47057 Duisburg, Germany

D. Koch
Institute of Materials Science
Technical University of Darmstadt
Alarich-Weiss-Str. 2, 64287 Darmstadt, Germany

A. R. Ziefuß
Technical Chemistry I and Center for Nanointegration Duisburg-Essen
(CENIDE)
University of Duisburg-Essen
Universitätsstr. 7, 45141 Essen, Germany

inconsistencies, and relatively low-material-deposition rates.^[25,26] Among the different printing technologies developed, laser printing provides advantages such as a micrometric spatial resolution,^[27–30] and a fast processing speed.^[31,32] The technique is based on the irradiation of the deposited ink with a tightly focused laser beam.^[33,34] It can be combined with different ink-deposition methodologies such as spin-coating or inkjet to sinter specific areas of the coated substrate and generate the desired continuous structures. The fast processing and localized energy delivery are advantages that allow thermally efficient heat transfer to the ink rather than the substrate, minimizing energy losses and permitting the use of inexpensive and/or low damage threshold substrates, which cannot bear high thermal loads during an extended time as required for oven sintering. Additionally, the short processing time reduces the risk of oxidation for the metallic inks,^[25] negating the need for an inert gas atmosphere or vacuum setup during the process.^[35] Laser printing has been used to fabricate printed electronics,^[36,37] as well as for tissue engineering,^[38,39] microfluidics,^[40,41] magnetic sensors,^[42,43] and holographic elements.^[44,45] Material properties such as microstructure, crystallographic structure, and magnetic and electric conductivity can be manipulated by controlling the laser and scanning parameters, affecting the induced sintering process by modifying the temperature reached and the cooling rate.

Compact and efficient miniaturized electronics-based and semiconductor-based devices encounter challenges such as high power dissipation and uneven temperature distribution, resulting from their high function-to-area ratio. These problems can shorten the device's shelf life and impact its overall performance.^[46] Various thermal management solutions have been investigated, such as design optimization of micro heat sinks,^[47] varying working coolants^[48,49] (such as nanofluids and dielectric coolants), and liquid flow system designs^[50] (single-phase flow or multiphase flow). However, the applicability of these approaches is limited because of the electric short-circuiting possibility (due to the leakage of liquid-based coolants), the difficulty of heat extraction from local hotspots, and the complex design of miniaturized devices (which requires precise manufacturing of heat sinks), overall making it difficult to reduce the temperature effectively.^[51]

Magnetocaloric materials have the potential to overcome the aforementioned limitations. These materials exhibit a temperature change when subjected to an external magnetic field, making them attractive for replacing compressed chlorofluorocarbon/fluorocarbon (CFC/FC) gas-based refrigeration systems.^[52–55] Compared to conventional cooling systems, magnetocaloric refrigeration is more environmentally friendly, quieter, and potentially more efficient.^[53,56] Furthermore, solid-state refrigeration is a viable option for miniaturized heat sinks, as it avoids leakage issues and efficiently extracts heat from hotspots. A number of materials have been investigated for magnetocaloric refrigeration across different temperature ranges.^[57–59] For example, $\text{La}(\text{FeSi})_{13}$ ^[60] displays a temperature change of 6.9 K at an operating temperature of 190 K, while Mn_3GaC ^[61] exhibits a temperature variation of 4.5 K at 163 K, and $\text{Gd}_2\text{Si}_2\text{Ge}_2$ ^[62] has a temperature change of 4.9 K at 262 K under an applied magnetic field of 2 T. These materials exhibit the most significant temperature change at the phase-

transition temperature, and their operating range and cooling capacity depend on the width and characteristics of their magnetic phase transition.

Among the series of magnetocaloric materials investigated so far, the equiatomic iron-rhodium (FeRh) alloy achieves the largest adiabatic temperature change ($\Delta T = 12.9$ K at $\Delta H = 2$ T) with an entropy change up to $16 \text{ J kg}^{-1} \text{ K}^{-1}$ at 308.2 K due to an anti-ferromagnetic to ferromagnetic (AFM–FM) first-order phase transition.^[63] However, the phase-transition temperature of FeRh is greatly influenced by the alloy's composition and the existence of defects in the crystal structure. As a result, it can take place in a broad range from room temperature to 400 K.^[64,65] This magnetoelastic transition does not lead to a change in crystallographic symmetry in the CsCl-type lattice structure (widely known as B2 structure), but is accompanied by significant magneto-structural volume expansion of about 1%.^[66] The cause of this transition is attributed to a significant alteration in the exchange interaction and elastic energy resulting from a modification in the crystal lattice parameter. Bean and Rodbell's exchange–striction model^[67] provides a viable method to simulate the underlying mechanism responsible for this transition. It has demonstrated strong consistency with theoretical and empirical data determining the magnetic characteristics of both the AFM and FM phases.^[68] Despite the fact that the material displays a significant magnetocaloric effect, the high cost of the alloy limit its application in bulk. Rhodium (belonging to the platinum group of metals) is among the rarest elements in the periodic table, with a price twice as high as platinum and seven times higher than palladium.^[69] Hence, its use in refrigeration systems requiring large amounts of bulk FeRh is limited by its availability and an associated price increase that a high industrial demand would imply. However, such alloys can be useful for the cooling of miniaturized devices, where a limited quantity is required.

Up to date, the synthesis of FeRh microparticles and NPs has been carried out mainly by wet chemical processes in the context of applications such as heat-assisted magnetic recordings, bio hyperthermia, and catalysis.^[70–73] Microsized FeRh alloys have shown an appreciable magnetocaloric effect,^[73] but their size limits the printing of structures with submicron or nanoscale resolution. Alternatively, FeRh NPs synthesized by a wet chemical process resulted in the inhomogeneous distribution of Fe and Rh in the NPs, which led to the coexistence of AFM and FM phases. In contrast, by using pulsed laser ablation in organic solvents, we created near-to-equiatomical γ -FeRh solid-solution NPs in a previous study.^[74] This current study builds on that work and employs laser printing to create magnetocaloric custom structures with micrometric dimensions, improving the sintering characteristics and magnetic phase conversion of the printed structures. Additionally, the magnetic and magnetocaloric properties of the laser-sintered structures are compared to those produced through standard industrial furnace sintering to optimize the magnetocaloric response of the sintered structures. The direct writing of magnetocaloric materials in this manner presents the opportunity to design a range of devices, including magnetic actuator systems, thermal switches, magnetic micropumps, and magnetic microcoolers.^[75,76]

2. Experimental Section

2.1. Synthesis of NPs and Ink Preparation and Deposition

Near-to-equimolar FeRh NPs were synthesized by laser ablation in liquids (LAL). LAL offers several benefits, including the ability to control the composition of the generated particles, and the potential to produce ligand-free NPs and tailored surface properties for a wide range of applications.^[77–79] This NP synthesis method found numerous applications in fields such as biomedicine,^[80,81] energy generation,^[82,83] and additive manufacturing,^[84,85] making it a versatile and promising technology. Here, the synthesis of the FeRh NPs was achieved by laser ablation of a Fe₅₀Rh₅₀ bulk target in ethanol employing a near-infrared picosecond (ps)-pulsed Nd:YAG solid-state laser source (Ekspla, Atlantic Series, Vilnius, Lithuania, 10 ps, 100 kHz, 80 μJ, 1064 nm). The ablation of the FeRh target was performed by focusing the laser beam with an $f=100$ mm lens on the FeRh target's surface, with the surface being scanned at 2 m s^{-1} (Figure 1a).^[74] The NP size distribution was analyzed by scanning electron microscopy (SEM) in the scanning transmission electron microscope (STEM) mode. The resulting NP size distribution is shown in (Figure S1, Supporting Information). The peak size obtained was 6.9 ± 3.0 nm with a polydispersity index of 0.4. The produced colloidal NPs (FeRh NPs in ethanol) were used to formulate a 1 wt% FeRh ink. This was done by partial evaporation of ethanol from the colloid at room temperature employing a 64 W axial fan with a flow rate of $925\text{ m}^3\text{ h}^{-1}$ (Figure 1b). Before the deposition of the ink, the glass substrates were processed in a UV cleaner for 5 min to remove any organic contaminations. The ink deposition on the substrate was performed by initially adding 200 μL of 10 wt% polyvinylpyrrolidone (PVP, MW = 40 k) in ethanol on the 25×75 mm glass substrate.

To avoid agglomeration, the FeRh ink was ultrasonicated for 10 min before the dispersion, 100 μL of FeRh ink were then dispersed on the area of $\approx 25 \times 15$ mm polymer-coated glass substrate (Figure 1c).

2.2. FeRh NP Ink Sintering

The sintering of NPs was conducted using a programmable furnace with separate runs in air and argon flow (Figure 1d). The glass substrates with the deposited ink were subjected to a heating rate of 10 K min^{-1} and reached a maximum temperature of 873 K, where they were held for 1 h. Following this, the furnace was turned off, and the substrates were left in the furnace to cool down to room temperature.

The laser sintering (Figure 1e) was carried out using a continuous wave (CW)-laser (Laser Quantum, 532 nm) and a programmable two-axis linear stage (Thorlabs DDSM100/M) on the ink-deposited glass substrates. The laser beam was focused by a microscope objective (Mitutoyo, 10X). The substrate was placed on the stage and was scanned in a single axis to achieve a sintered line. For characterization techniques that required larger areas of study, the X–Y stage was programmed to produce successive parallel lines such that all the regions between the lines were irradiated, covering the whole ink-dispersed region. The laser-sintered custom patterns were obtained by programming the linear stage in both the X and Y axes, leading to the sintering of the desired areas of the deposited ink. The substrate was then dispersed in an ethanol bath and ultrasonicated for 5 min, removing all the non-sintered ink and polymer layers.

The laser fluence was varied to evaluate the material-sintering window, and was calculated using the following formula^[86]

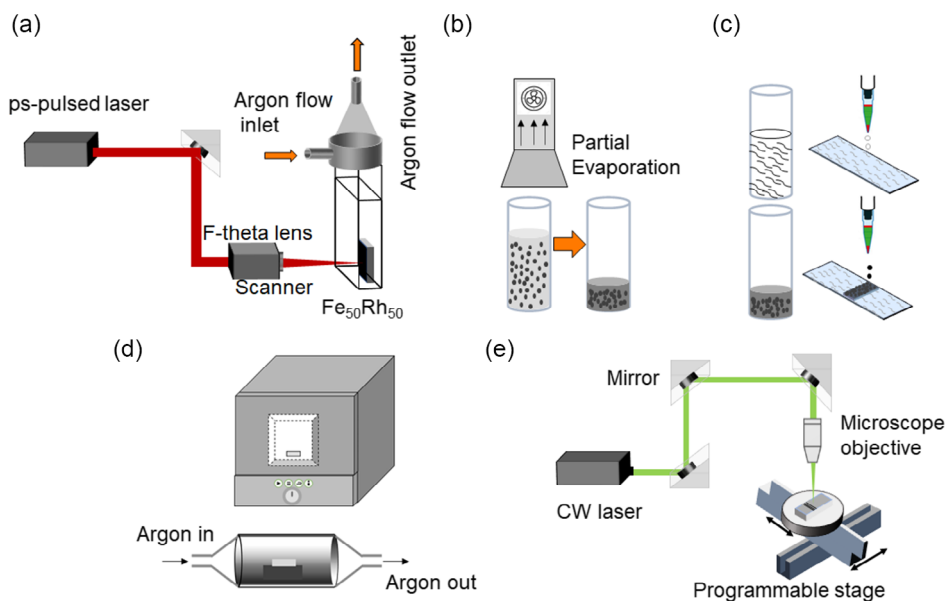


Figure 1. Schematic step-by-step process for sintering of near-to equimolar FeRh nanoparticles (NPs). a) Synthesis of NPs by picosecond (ps)-pulsed laser ablation in ethanol in a Schlenk chamber. b) Partial evaporation of ethanol from the FeRh NP colloid employing an axial fan at room temperature. c) Deposition of polyvinylpyrrolidone (PVP, MW = 40 000) and FeRh ink on a selected region of the glass substrate. d) FeRh nanoink sintering by programmable furnace in air and furnace with argon flow. e) Sintering by 532 nm continuous wave laser and a microscope objective (10×) providing the micrometric resolution required.

$$F = \frac{4 \cdot P}{v_s \cdot d \cdot \pi} \quad (1)$$

where F = laser fluence, P = laser power, v_s = scanning speed, and d = laser spot diameter. The scanning speed was kept constant at 10 mm s^{-1} for all the experiments and the laser fluence was varied between 16 and 246 J cm^{-2} . The sintered micrometric lines were visualized by an optical microscope (Leica DM2700 M) and SEM (Apreo S LoVac, Thermo Fisher Scientific). The width was measured using ImageJ software at ten different positions on each line.

The laser processing at high fluences resulted in FeRh NP ablation along with the sintering (explained later in detail), enhancing the porosity of the magnetocaloric structures. The effect of laser fluence on the ablation of FeRh ink was monitored by reflectance spectroscopy (Supporting Information). The effect of laser-induced heating and furnace heating on the FeRh crystal structure was studied by X-ray diffraction (XRD) in θ - 2θ geometry with Cu-K α radiation using a Philips PW1730 X-ray diffractometer with a graphite monochromator, aiming to quantify the phase conversion achieved during the sintering processes. Rietveld refinement was carried out using the Fullprof suite.^[87] The B2 fraction was also analyzed based on magnetometry data of the FeRh ink after laser and furnace sintering, to determine the sintering parameters yielding the highest B2-phase fraction. $M(H)$ curves were measured using the vibrating-sample magnetometer (VSM) option of a PPMS DynaCool (Quantum Design) between 5 and 400 K and up to a maximum of 500 K using a VSM oven option in magnetic fields up to 9 T and were corrected for the distinct dia- and paramagnetic glass substrate background signal; $M(T)$ measurements were performed between 150 and 700 K at an applied field of 0.1 T.

3. Results and Discussion

3.1. FeRh NP Ink Sintering

To examine the morphology of the sintered structures within different laser fluence regimes, optical microscopy and SEM were used, as shown in **Figure 2**. Initially, the ink is partially sintered leading to the formation of a discontinuous line pattern

consisting of sintered and non-sintered regions (**Figure 2a**). The laser interaction leads to the NP densification and partial evaporation of the polymer. Increasing the laser fluence above 16 J cm^{-2} results in the formation of necks and percolation networks start to grow. At a laser fluence of 41 J cm^{-2} , the NPs are sintered, forming a homogenous line with a dense magnetocaloric structure (**Figure 2b**). Increasing the fluence to 57 J cm^{-2} results in the creation of compact agglomerates of NPs, attributed to fusion, grain growth, and lattice diffusion.^[88] The increase in laser energy also leads to ablation along with sintering, mainly at the center of the line, where the intensity is the highest, resulting in distinct network structures rather than continuous NP films (**Figure 2c**). At higher fluences, NP ablation is more pronounced and the overall density of the dispersed NP layer is reduced (**Figure 2d**). The ablation causes an increase in the porosity of the magnetocaloric structure, which could potentially enhance the convective heat transfer to the working fluid in magnetocaloric regenerators.^[89]

We also examined the morphology of FeRh ink furnace sintered at 873 K for 1 h. Compared to laser processing, the furnace-sintered NPs appeared more compact due to the slow heating rate and uniform temperature distribution (as shown in **Figure 3**). The gradual heating rate provided sufficient time for particle migration, promoting uniform sintering throughout the NP film, and to avoid the formation of individual networks of structures. The slow heating and cooling process may have resulted in surface oxidation due to residual oxygen, which could have a negative impact on the mechanical and magnetic properties of the sintered structures (as noted in Ref. [25]).

The optical microscopy and SEM results obtained from the laser-processed FeRh magnetocaloric ink can be explained by analyzing the intensity profile of the CW laser used in the process. The Gaussian intensity distribution of the laser defines various interaction regimes. At low fluence (16 J cm^{-2}), only a small region at the center of the line is above the threshold intensity required for sintering (shown by the extrapolated dashed line (**Figure 4a**)). Latter depicts the width of the line for each peak intensity. The line width increases upon increasing laser fluence (**Figure 4b**), which is also visualized by the black arrows in the optical microscopy images (**Figure 2**). For a sintered line (41 J cm^{-2}), the peak intensity of the Gaussian beam lies below the ablation threshold with a significant area of the Gaussian

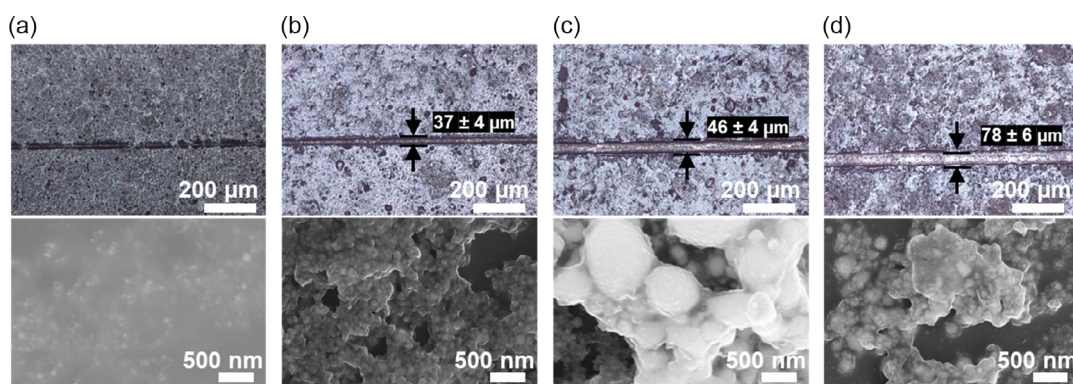


Figure 2. Surface morphology of laser-sintered structures of FeRh NPs after applying different laser fluences as visualized by optical microscopy and scanning electron microscopy: a) 16 J cm^{-2} , b) 41 J cm^{-2} , c) 57 J cm^{-2} , and d) 246 J cm^{-2} . The black arrows show the width of the sintered line.

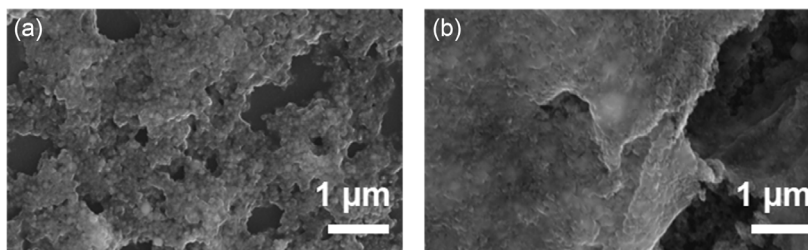


Figure 3. SEM images of the sintered FeRh NP ink surface morphology for a) laser sintering at a fluence of 41 J cm^{-2} , and b) a furnace-sintered structure at 873 K for 1 h.

distribution above the sintering threshold. At higher fluences, the ablation of NPs is observed along with sintering mainly in the central region of the lines where the intensity of the laser beam is the highest (Figure 2c,d). At higher fluences, the ablation of NPs is observed along with sintering mainly in the central region of the lines, where the intensity of the laser beam is the highest (Figure 2c,d). The ablation regimes can be analyzed by reflectance spectroscopy, as depicted in Figure S2, Supporting Information. The partial ablation of the ink resulted in the formation of porous structures confirmed by an increased optical transmission (Figure S3, Supporting Information). The maximum fluence that could be achieved without substrate damage was 246 J cm^{-2} . Although the line width increases with an increasing laser fluence, it saturates at 246 J cm^{-2} , limited by the Gaussian beam's shape and diameter.

3.2. Structural and Magnetic Characterization of the Magnetocaloric Microstructures

Annealing FeRh NPs induces a phase transition from the γ to the B2 phase, which is essential to enhance the material's magnetic and magnetocaloric properties.^[74] To investigate the effect of laser-assisted heating and furnace heating on the crystal structure and phase formation of FeRh NP ink, we performed XRD experiments. Figure 5a shows the diffraction patterns

indicating a phase change from the γ phase to a mixed B2- γ state as the laser fluence is increased. The B2-, γ -, and Fe_xO_y -molar-phase fractions were evaluated via Rietveld refinement (Figure 5c). The furnace-based annealing in air at 873 K leads to a complete transformation to the Fe_2O_3 (hematite) phase, while annealing in argon-flow results in a mixture of B2 and γ phase and a minor Fe_3O_4 (magnetite) contribution (Figure 5c). However, a lower degree of oxidation was observed for laser-processed inks and was mainly evident for laser fluences lower than 131 J cm^{-2} (Figure 5a marked with asterisk). The overall phase fraction shows that the B2 phase increases and the γ phase is reduced with increasing laser fluence, as summarized in Table 1. This shows that the laser-sintering technique not only leads to higher γ - to B2-phase conversion, but also represents a more oxidation-resistant process than a conventional one. This is a remarkable fact considering that laser sintering is performed in air, hence avoiding the time and resource-costly employment of inert gas atmospheres. Additionally, the high laser fluences lead to NP ablation, giving rise to the formation of micropores, which could be essential for heat transfer to the cooling media for magnetocaloric regenerators. For the laser-sintered sample, a small splitting of the reflections of the γ phase appears at some samples, indicating two γ -phases with different lattice parameters. This can be explained by hydrogen, which is incorporated into the structure during NP synthesis,^[74] being released, resulting in a contraction of the lattice.^[74]

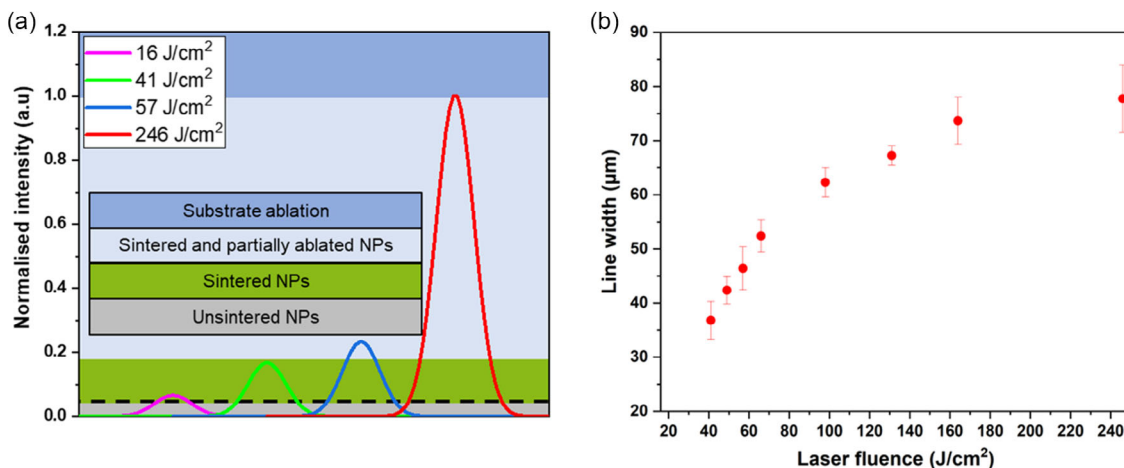


Figure 4. a) Gaussian intensity profile at laser fluences (ranging from 16 to 246 J cm^{-2}) showing the unsintered, sintered, and ablation regimes. The dashed line (black) indicates the width of the sintered line. b) Laser fluence effect (ranging from 41 to 246 J cm^{-2}) on the line width of the sintered magnetocaloric structures. The error bar shows the standard deviation of line widths measured at the 10 different positions of each sintered line.

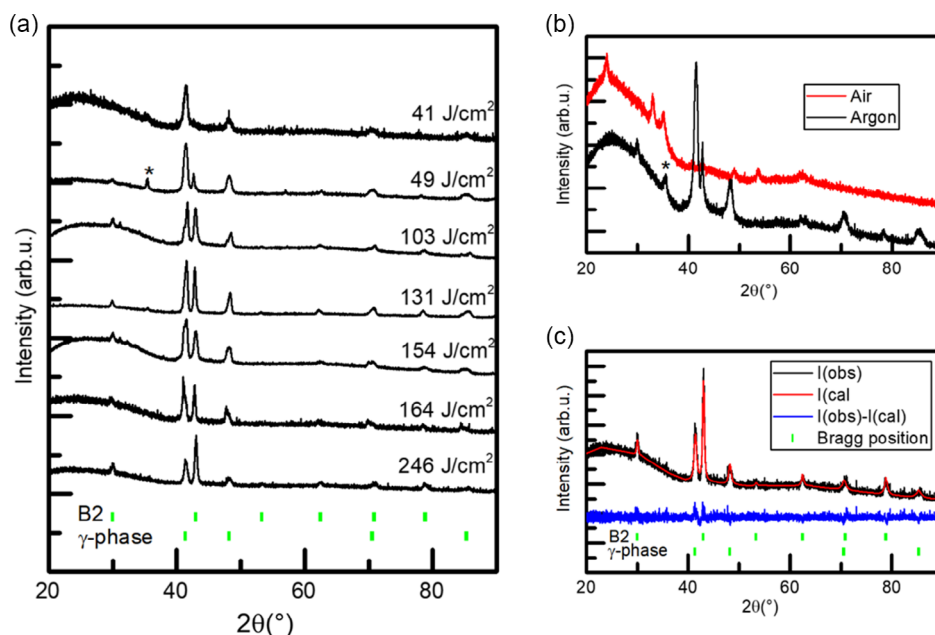


Figure 5. a) X-ray diffraction (XRD) data of laser-sintered samples with fluences from 41 to 246 J cm⁻². The tick marks indicate the possible position of reflections for the B2 phase and the γ phase. Reflections from oxide impurities are marked with an asterisk. b) Comparison of furnace-sintered samples on air and Ar atmosphere. c) Rietveld refinement of the laser-sintered sample with an fluence of 246 J cm⁻².

Table 1. Molar fraction of main crystalline phases of furnace-sintered and laser-sintered samples determined by XRD, estimated by Rietveld refinements.

Process	Parameters	B2-molar-phase fraction	γ-molar-phase fraction	Fe _x O _y -molar-phase fraction
Furnace sintering	873 K in air	–	–	1.00 (Fe ₂ O ₃)
Furnace sintering	873 K in argon	0.08	0.65	0.27 (Fe ₃ O ₄)
Laser sintering	41 J cm ⁻²	–	1.00	–
Laser sintering	49 J cm ⁻²	0.08	0.74	0.18 (Fe ₃ O ₄)
Laser sintering	103 J cm ⁻²	0.38	0.62	–
Laser sintering	131 J cm ⁻²	0.29	0.67	0.04 (Fe ₃ O ₄)
Laser sintering	154 J cm ⁻²	0.29	0.71	–
Laser sintering	164 J cm ⁻²	0.30	0.70	–
Laser sintering	246 J cm ⁻²	0.52	0.48	–

The magnetization response of the laser sintered as well as furnace-annealed FeRh NPs is studied via magnetometry regarding composition and the AFM–FM phase transition in direct comparison to XRD data analysis. Field-dependent magnetization curves of FeRh ink laser-irradiated at fluences of 41 up to 246 J cm⁻² recorded at 500 K are shown in Figure 6a. Higher laser fluences result in an increase of the saturation magnetization M_S , which hints toward a partial phase transformation from paramagnetic γ-FeRh to FM B2-FeRh. For fluences lower than 131 J cm⁻², different magnetic alignment behavior is observed in the low-field region, together with slightly increased coercive fields. Both effects can be assigned to partial oxidation to a

magnetite/maghemite phase, accompanied by an increase in total magnetization.

Magnetization $M_{(500\text{ K}, 2\text{ T})}$ values extracted from the measurements at 500 K and 2 T are compared to B2 fractions obtained in XRD analysis in Figure 6b. Since the FeRh-sintered structures are in the FM state above the phase transition at 500 K, the magnetization is expected to be representative for the B2-FeRh fraction of the sample (in case no oxides are present). In fact, a general agreement between XRD B2 fraction and $M_{(500\text{ K}, 2\text{ T})}$ can be observed, not including partially oxidized samples, where a magnetite fraction results in deviating magnetization values. Furthermore, it has to be considered that a direct determination of the remaining FeRh mass on the samples after laser treatment could not be performed, wherefore it was estimated based on the total amount of deposited FeRh material in relation to the area of the sample pieces studied in magnetometry, where minor inhomogeneities in NP coverage can increase the error margin. Disregarding samples with considerable oxide fraction, high-field magnetization $M_{(500\text{ K}, 2\text{ T})}$ and B2-phase fraction display a comparable trend in laser fluence assuming a saturation magnetization of $\approx 100\text{ Am}^2\text{ kg}^{-1}$, matching the range of reported values for pure B2-FeRh at 500 K.^[90]

The magnetization of laser-treated FeRh-deposited ink was compared to those from the conventional annealing processes. The FeRh inks deposited on glass substrate were subjected to elevated temperatures of 573–873 K under ambient air or argon atmosphere, respectively (Figure 7). After annealing in air, oxidation of the original γ-FeRh phase resulted in the formation of hematite (as also observed in XRD). This is clearly visible by the changes in the $M(H)$ shape and by the decreasing high-field magnetization due to the canted AFM structure of hematite. In contrast, annealing of the FeRh NPs under argon atmosphere results

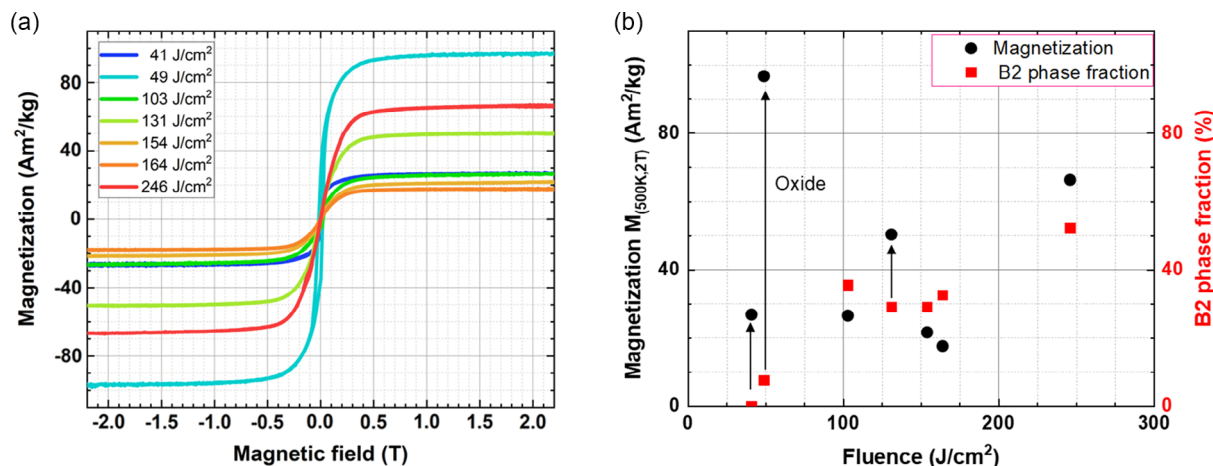


Figure 6. a) Field-dependent magnetization at 500 K of FeRh NPs deposited on glass substrate after laser sintering using fluences of 41 up to 246 J cm⁻². b) FeRh magnetization $M_{(500\text{K}, 2\text{T})}$ (black) was recorded at 500 K at 2 T (black dots) compared to B2-phase fractions (red) as determined from XRD analysis. The arrows indicate the samples whose magnetization was increased due to partial oxidation, that is, formation of magnetite, as indicated by XRD results.

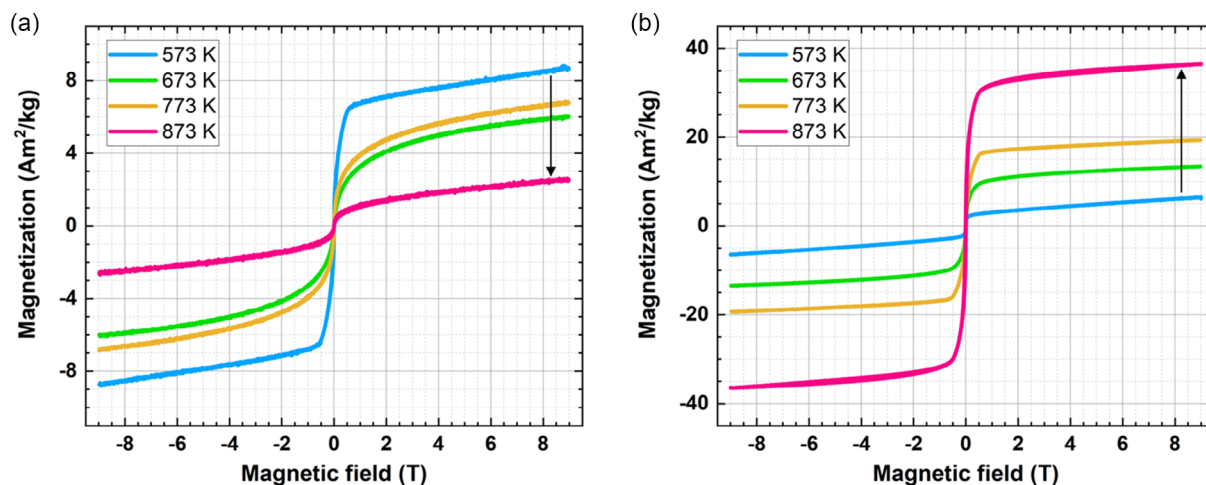


Figure 7. Field-dependent magnetization of FeRh NPs deposited on glass substrate at 300 K after annealing at $T_H = 573$ to 873 K in a) air or b) argon, respectively.

in the conservation of the $M(H)$ shape, showing predominant magnetic alignment already at 0.5 T, combined with a continuous increase in magnetization upon increasing annealing temperature in reaction to γ - to B2-FeRh conversion, as seen in XRD data. The annealing under argon atmosphere results in much higher B2 fraction and, accordingly, higher magnetization, by preventing any oxidation of the FeRh material to hematite as observed under annealing in air. Comparing the conventional annealing processes in the furnace with laser sintering, highest mass magnetization values obtained via laser-sintering FeRh ink exceed that of furnace-sintered samples, while also allowing the simultaneous printing/writing of 2D structures.

Previous experiments on FeRh NP powder showed similar results to those of the argon-flow annealing discussed earlier, with almost complete conversion of the γ -FeRh phase to the

B2 structure.^[91] Still, while high B2 fractions were obtained, magnetization and Mössbauer spectroscopy experiments indicated only a moderate fraction of the FeRh material to participate in the AFM–FM phase transitions, being primarily pinned in a ferromagnetic state. To study the laser-based sintering route under this aspect, field-dependent magnetization behavior was analyzed across the phase-transition temperature in detail for the laser fluence of 246 J cm⁻², which showed the maximum B2 fraction and magnetization.

3.3. Magnetocaloric Properties

FeRh ink laser sintered with a laser fluence of 246 J cm⁻² displays considerable magnetization already below the AFM phase transition at 150 K (Figure 8). This is in agreement with the observation of a partial-pinned ferromagnetic state of FeRh

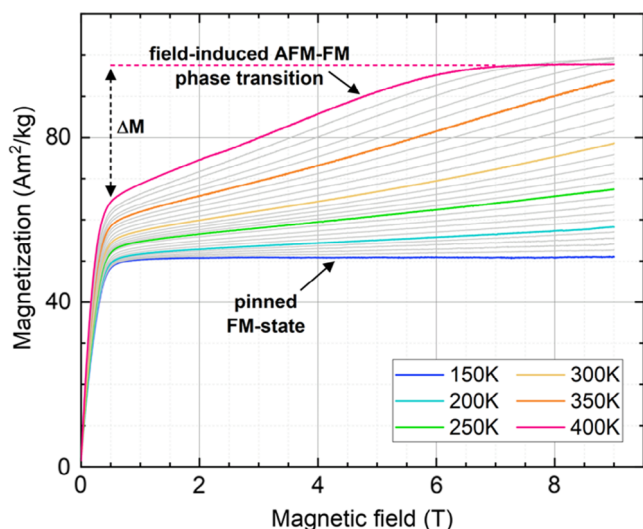


Figure 8. Magnetization of FeRh NPs deposited on glass substrate and laser sintered at a fluence of 246 J cm^{-2} measured from 0 to 9 T at 150 up to 400 K across the antiferromagnetic to ferromagnetic (AFM–FM) phase transition. The contribution of FeRh material pinned in the FM state as well as the increase in magnetization ΔM connected to the field-induced AFM–FM transition is indicated by arrows.

NPs after annealing.^[65] Possible explanations for a partially pinned ferromagnetic fraction include a minor variation in stoichiometry in the NPs produced via LAL, as even miniscule variations of the Fe content in FeRh can cause considerable changes in the AFM–FM phase-transition temperature or even the permanent conservation of ferromagnetic behavior. Also, structural defects in the FeRh lattice are known to stabilize ferromagnetic order, as shown before by inducing different degrees of structural disorder via ion irradiation,^[92] which could be present in the FeRh NPs after the laser-ablation process.

At higher temperatures, $M(H)$ data shows an increase in magnetization upon rising fields, assigned to the beginning of the AFM–FM transition already at $\approx 150\text{--}200 \text{ K}$ due to substantial broadening of the transition. A measurement of temperature-dependent magnetization was recorded at 0.1 T to illustrate the sample behavior across the phase transition (Figure S4, Supporting Information), which indicates that the AFM–FM phase-transition peak was achieved at $\approx 460 \text{ K}$, where all FeRh can be considered as ferromagnetic. Here, it has to be noted that minor changes in $M(H)$ are superpositioned by a temperature-dependent decrease in the background signal of the employed glass substrate (already subtracted from the data in Figure 8). Due to the very limited net magnetic moment of the FeRh thin layer as compared to the substrate material, even minor uncertainties regarding background subtraction can result in slightly different $M(H)$ shapes in this temperature region. Above $\approx 250\text{--}350 \text{ K}$, $M(H)$ shows a more distinct nonlinear increase in field-dependent magnetization when approaching the bulk-phase-transition temperature where most of the FeRh NPs reach the ferromagnetic state. At 400 K, a constant magnetization value of $\approx 98 \text{ Am}^2 \text{ kg}^{-1}$ is reached above 7 T, as the transition to the FM state is completed, with the distinct field-driven increase in magnetization of about $\Delta M = 35 \text{ Am}^2 \text{ kg}^{-1}$

corresponding to the field-induced phase transition. Comparing these results to previous experiments on furnace-annealed FeRh NPs ($\Delta M = 6 \text{ Am}^2 \text{ kg}^{-1}$),^[91] a much higher field-driven increase in magnetization is observed following the laser-sintering route, being evidence of the potential of laser-written 2D structures for magnetocaloric applications. Although a more detailed analysis is hindered by the considerable para- and diamagnetic background contribution of the glass substrate, a value of $\approx 3\text{--}3.5 \text{ J kg}^{-1} \text{ K}^{-1}$ can be extracted from the data as a rough estimate of the change in magnetic entropy connected to the AFM–FM phase transition between 0 and 9 T, as is elucidated in more detail in the corresponding section of Supporting Information (Figure S5, Supporting Information). Further improvement in magnetocaloric performance is expected under optimization of laser-ablation and especially laser-sintering parameters by increasing attainable B2-FeRh fractions and reducing ferromagnetic pinning.

3.4. Custom FeRh Magnetocaloric Microstructures by Laser Sintering

Evaluating the magnetic properties of the FeRh structures after sintering indicated that laser sintering (at a fluence of 246 J cm^{-2}) of the FeRh NP ink leads to a higher conversion to magnetic phases and decreases the possibility of FeRh NP oxidation compared to furnace sintering, due to the rapid heating and cooling process occurring during laser sintering. The laser-sintering process provides inherent spatial resolution and scanning flexibility that enables the creation of customized magnetocaloric microstructures, as demonstrated in Figure 9a. After processing the desired spatial pattern, the unsintered ink can be removed by cleaning with the ink solvent (ethanol), resulting in sintered structures remaining on the substrate (as depicted in Figure 9b). The quality of the laser-sintered FeRh structures, coupled with the ability to attain accurate spatial resolution and design customized geometries, make this technique a promising method for producing micrometric cooling structures for miniaturized electronic devices in particular when compared to furnace sintering.

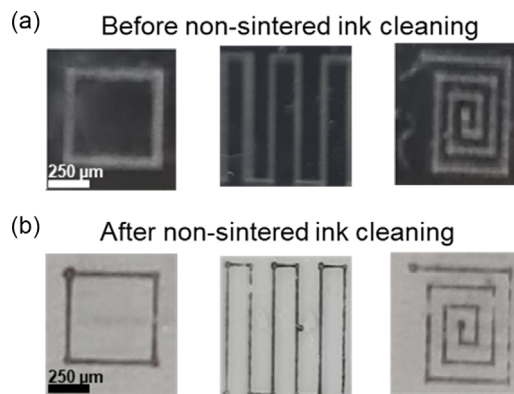


Figure 9. Depiction of the custom structures produced through laser processing at a laser fluence of 246 J cm^{-2} , with showing the structures a) before cleaning of the deposited FeRh ink and b) after cleaning with ethanol using ultrasonication for 5 min. The scale bar remains consistent across all images.

4. Conclusion

Producing micrometric magnetocaloric devices presents a promising avenue for creating compact cooling sources. In this study, we have outlined a sequential process for fabricating FeRh magnetocaloric custom structures starting with the laser-based NP synthesis employing a bulk target, followed by ink formulation, dispersion on substrate, and sintering of NP ink employing a CW laser. The CW laser sintering of the NP ink was evaluated to define the processing window. The NPs were completely sintered at 41 J cm^{-2} with further increase in the laser fluence that promotes ablation of NPs along with sintering. This results in the increase of porosity of the magnetocaloric structure, which could promote the convective heat transfer to the working fluid for magnetic regenerators.

The laser-induced heating resulted in a partial phase transformation from γ to B2 phase, with the maximum B2 fraction being 52%. This transformation caused a magnetization increase of $\approx 66 \text{ Am}^2 \text{ kg}^{-1}$ and a maximum rise in magnetization of approximately $35 \text{ Am}^2 \text{ kg}^{-1}$ across the field-driven AFM–FM phase transition. Compared to oven sintering, laser sintering facilitated faster processing, prevented oxidation, enabled the formation of intricate micrometric patterns, and improved the magnetocaloric phase transformation.

Supporting Information

Supporting Information is available from the Wiley Online Library or from the author.

Acknowledgements

The authors thank Tobias Bochmann for his help with the SEM imaging of sintered samples. The authors gratefully acknowledge the funding by the German Research Foundation (DFG) within the Collaborative Research Centre/Transregio (CRC/TRR) 270 (Project-ID 405 553 726, projects A11, B04, B05, and B08), as well as the CRC/TRR 247 (Project-ID 388 390 466, project B02). Bilal Gökce further thanks the DFG for funding of the project GO 2566/10-1.

Open Access funding enabled and organized by Projekt DEAL.

Conflict of Interest

The authors declare no conflict of interest.

Data Availability Statement

The data that support the findings of this study are available from the corresponding author upon reasonable request.

Keywords

antiferromagnetic–ferromagnetic phase transition, iron–rhodium, laser ablation in liquid, laser sintering, micro cooling

Received: February 21, 2023

Revised: April 19, 2023

Published online: May 17, 2023

- [1] T. Dullweber, S. Gatz, H. Hannebauer, T. Falcon, R. Hesse, J. Schmidt, R. Brendel, *Prog. Photovoltaics* **2012**, *20*, 630.
- [2] M. M. Hilali, J. M. Gee, P. Hacke, *Sol. Energy Mater. Sol. Cells* **2007**, *91*, 1228.
- [3] D. C. Nguyen, S. Ito, *Int. J. Nanotechnol.* **2013**, *10*, 269.
- [4] L. Z. Li, G. Tang, Z. Shi, H. Ding, C. B. Liu, D. L. Cheng, Q. Y. Zhang, L. Yin, Z. B. Yao, L. Duan, D. H. Zhang, C. G. Wang, M. X. Feng, Q. Sun, Q. Wang, Y. J. Han, L. Wang, Y. Luo, X. Sheng, *Proc. Natl. Acad. Sci. USA* **2021**, *118*, e2023436118.
- [5] Z. Bao, J. W. Luo, Y. S. Wang, T. C. Hu, S. Y. Tsai, Y. T. Tsai, H. C. Wang, F. H. Chen, Y. C. Lee, T. L. Tsai, R. J. Chung, R. S. Liu, *Chem. Eng. J.* **2021**, *426*, 130849.
- [6] G. Vescio, J. L. Friero, A. F. Gualdron-Reyes, S. Hernandez, I. Mora-Sero, B. Garrido, A. Cirera, *Adv. Mater. Technol.* **2022**, *7*, 2101525.
- [7] M. Montanino, G. Sico, A. D. Del Mauro, J. Asenbauer, J. R. Binder, D. Bresser, S. Passerini, *Energy Technol.* **2021**, *9*, 2100315.
- [8] M. A. Nazri, L. M. Lim, Z. Samsudin, M. Y. T. Ali, I. Mansor, M. I. Suhaimi, S. R. Meskon, A. N. Nordin, *3D Print. Addit. Manuf.* **2021**, *8*, 176.
- [9] P. H. Yang, J. Li, S. W. Lee, H. J. Fan, *Adv. Sci.* **2022**, *9*, 2103894.
- [10] Y. Z. Li, Y. X. Liu, S. R. A. Bhuian, Y. Zhu, S. S. Yao, *Small Struct.* **2022**, *3*, 2100131.
- [11] R. Rayhana, G. G. Xiao, Z. Liu, *IEEE Trans. Instrum. Meas.* **2021**, *70*, 1.
- [12] E. Wawrzyniek, C. Baumbauer, A. C. Arias, *Sensors* **2021**, *21*, 6557.
- [13] Y. H. Xu, F. Y. Zhang, W. J. Zhai, S. J. Cheng, J. H. Li, Y. Wang, *Polymers* **2022**, *14*, 566.
- [14] Y. X. Zhou, W. Grayson, *MRS Bull.* **2022**, *47*, 91.
- [15] P. J. Wang, Y. Z. Sun, X. Q. Shi, H. X. Shen, H. H. Ning, H. T. Liu, *Bio Des. Manuf.* **2021**, *4*, 344.
- [16] S. H. Lee, S. Lee, *Polymers* **2019**, *11*, 245.
- [17] T. H. Phung, A. N. Gafurov, I. Kim, S. Y. Kim, K. M. Kim, T.-M. Lee, *Sci. Rep.* **2021**, *11* 19982.
- [18] M. Smolka, S. Ruttloff, D. Nees, C. Priel, V. Satzinger, B. Lamprecht, P. Hütter, J. Hesse, G. Kokkinis, G. Kriechhammer, D. Scheidl, B. Wilfing, *Proceedings* **2018**, *2*, 1054.
- [19] S. Park, H. Kim, J.-H. Kim, W.-H. Yeou, *Materials* **2020**, *13*, 3587.
- [20] P. M. Grubb, H. Subbaraman, S. Park, D. Akinwande, R. T. Chen, *Sci. Rep.* **2017**, *7*, 1202.
- [21] P. Zhang, F. Wang, M. Yu, X. Zhuang, X. Feng, *Chem. Soc. Rev.* **2018**, *47*, 7426.
- [22] K. Y. Mitra, A. Willert, R. Chandru, R. R. Baumann, R. Zichner, *Adv. Eng. Mater.* **2020**, *22*, 2000547.
- [23] A. Jo, S. I. Chung, P. K. Kim, J.-W. Lee, H. Lee, J. H. J. Yang, T.-G. Ha, J. Kim, Y. J. Lee, H. J. Jeong, S. H. Seo, S. Y. Jeong, G.-W. Lee, K.-J. Baeg, J. T. Han, J. H. Park, *ACS Appl. Energy Mater.* **2021**, *4*, 13666.
- [24] D. Ma, S. Chon, S. Cho, Y. Lee, M. Yoo, D. Kim, D. Y. Lee, J. K. Lim, *J. Electroanal. Chem.* **2020**, *876*, 114720.
- [25] J. Niittynen, M. Mäntysalo, *IEEE Trans. Compon. Packag. Manuf. Technol.* **2014**, *4*, 2018.
- [26] J. Jones, D. Büttner, R. Chudasama, D. Wimpenny, K. Krüger, *J. Imaging Sci. Technol.* **2012**, *56*, 40503.
- [27] Y. P. Kathuria, *1997 Int. Symp. on Micromechanics and Human Science (Cat. No. 97TH8311)*, October 1997, pp. 41–47.
- [28] J. H. Park, J. W. Lee, Y. W. Ma, B. S. Kang, S. M. Hong, B. S. Shin, *Nanomaterials* **2022**, *12*, 387.
- [29] Y. P. Yuan, Z. Liu, K. H. Zhang, W. N. Han, J. M. Chen, *Opt. Laser Technol.* **2018**, *103*, 327.
- [30] A. Hurtado, D. Jevtics, B. Guilhabert, Q. Gao, H. H. Tan, C. Jagadish, M. D. Dawson, *IET Optoelectron.* **2018**, *12*, 30.
- [31] N. K. Roy, D. Behera, O. G. Dibua, C. S. Foong, M. A. Cullinan, *Microsyst. Nanoeng.* **2019**, *5*, 64.
- [32] A. Nazir, J.-Y. Jeng, *Proc. Inst. Mech. Eng. Part C* **2019**, *234*, 2741.

- [33] M. Feinäugle, R. Eason, C. Sones, B. Mills, J. A. Grant-Jacob, I. Katis, D. J. Heath, Making Additive Manufacturing Functional - The Laser-Assisted Fabrication of Electronic and Photonic Devices, **2014**.
- [34] D. Lowell, D. George, J. Lutkenhaus, C. Tian, M. Adewole, U. Philipose, H. L. Zhang, Y. K. Lin, *Micromachines* **2016**, *7*, 128.
- [35] I. I. Tumkin, E. M. Khairullina, M. S. Panov, K. Yoshidomi, M. Mizoshiri, *Materials* **2021**, *14*, 2493.
- [36] F. Zacharatos, M. Makrygianni, R. Geremia, E. Biver, D. Karnakis, S. Leyder, D. Puerto, P. Delaporte, I. Zergioti, *Appl. Surf. Sci.* **2015**, *374*, 117.
- [37] A. F. Harper, P. J. Diemer, O. D. Jurchescu, *npj Flexible Electron.* **2019**, *3*, 11.
- [38] R. K. Jayne, M. Ç. Karakan, K. Zhang, N. Pierce, C. Michas, D. J. Bishop, C. S. Chen, K. L. Ekinci, A. E. White, *Lab Chip* **2021**, *21*, 1724.
- [39] Y. Nahmias, R. E. Schwartz, C. M. Verfaillie, D. J. Odde, *Biotechnol. Bioeng.* **2005**, *92*, 129.
- [40] J. Xu, Y. Liao, J. Lin, Y. Zhong, X. Li, C. Jing, Y. Cheng, *Laser-based Micro- and Nanoprocessing XII* **2018**, p. 6.
- [41] J. Álvarez-Martínez, O. Medina-Cázares, M. Soto-Alcaraz, R. Castaneda-Priego, G. Gutierrez-Juarez, R. Castro-Beltrán, *J. Micromech. Microeng.* **2022**, *32*, 065001.
- [42] X. Zhang, H. Hu, D. Tang, C. Zhang, J. Fu, P. Zhao, *Sens. Actuators A: Phys.* **2021**, *327*, 112753.
- [43] D. Zhang, H. Wei, H. Hu, S. Krishnaswamy, *APL Photonics* **2020**, *5*, 076112.
- [44] Q.-Z. Zhao, J.-R. Qiu, X.-W. Jiang, E.-W. Dai, C.-H. Zhou, C.-S. Zhu, *Opt. Express* **2005**, *13*, 2089.
- [45] B. AlQattan, J. Doocey, M. Ali, I. Ahmed, A. E. Salih, F. Alam, M. Bajgrowicz-Cieslak, A. K. Yetisen, M. Elsherif, H. Butt, *ACS Nano* **2021**, *15* 2340.
- [46] T. Dixit, I. Ghosh, *Renewable Sustainable Energy Rev.* **2015**, *41*, 1298.
- [47] H. E. Ahmed, B. H. Salman, A. S. Kherbeet, M. I. Ahmed, *Int. J. Heat Mass Transf.* **2018**, *118*, 129.
- [48] T. Ikyumbur, F. Gbaour, S. Ochi, *Curr. J. Appl. Sci. Technol.* **2019**, *32*, 1.
- [49] M. Ali, A. M. El-Leathy, Z. Al-Sofyany, *Adv. Mech. Eng.* **2014**, *6*, <https://doi.org/10.1155/2014/962510>.
- [50] Y. Joshi, Z. Wan, *Handbook of Thermal Science and Engineering* (Ed: F. A. Kulacki), Springer International Publishing, Cham **2017**, pp. 1.
- [51] Z. He, Y. Yan, Z. Zhang, *Energy* **2021**, *216*, 119223.
- [52] J. Lyubina, *J. Phys. D-Appl. Phys.* **2017**, *50*, 053002.
- [53] A. Alahmer, M. Al-Amayreh, A. O. Mostafa, M. Al-Dabbas, H. Rezk, *Energies* **2021**, *14*, 4662.
- [54] H. L. Hou, S. X. Qian, I. Takeuchi, *Nat. Rev. Mater.* **2022**, *7*, 633.
- [55] A. Waske, M. Gruner, T. Gottschall, O. Gutfleisch, *MRS Bull.* **2018**, *43*, 269.
- [56] S. Fähler, U. K. Rößler, O. Kastner, J. Eckert, G. Eggeler, H. Emmerich, P. Entel, S. Müller, E. Quandt, K. Albe, *Adv. Eng. Mater.* **2012**, *14*, 10.
- [57] J. Y. Law, V. Franco, *J. Mater. Res.* **2022**, *38*, 37.
- [58] C. B. N. Kadiyala, N. Ram, M. Prakash, N. Uppara, S. K. Nagasamudram, S. Sarmash, T. Subbarao, R. Kumar, G. Kumar, *J. Supercond. Novel Magn.* **2018**, *31*, 1971.
- [59] W. H. Zhu, L. Ma, M. F. He, Z. K. Li, H. Z. Zhang, Q. R. Yao, G. H. Rao, K. P. Su, X. C. Zhong, Z. W. Liu, X. Q. Gao, *Adv. Eng. Mater.* **2023**, *2201770*, <https://doi.org/10.1002/adem.202201770>.
- [60] X. Chen, Y. Chen, Y. Tang, D. Xiao, *J. Rare Earths* **2015**, *33*, 1293.
- [61] F. Scheibel, T. Gottschall, K. Skokov, O. Gutfleisch, M. Ghorbani-Zavareh, Y. Skourski, J. Wosnitza, Ö. Çakır, M. Farle, M. Acet, *J. Appl. Phys.* **2015**, *117*, 233902.
- [62] V. K. Pecharsky, J. K. A. Gschneidner, *Phys. Rev. Lett.* **1997**, *78*, 4494.
- [63] M. Annaorazov, K. A. Asatryan, G. Myalikgulyev, S. A. Nikitin, A. M. Tishin, A. L. Tyurin, *Cryogenics* **1992**, *32*, 867.
- [64] J. B. Staunton, R. Banerjee, M. Dias, A. Deak, L. Szunyogh, *Phys. Rev. B* **2014**, *89*, 054427.
- [65] V. I. Zverev, A. M. Saletsky, R. R. Gimaev, A. M. Tishin, T. Miyanaga, J. B. Staunton, *Appl. Phys. Lett.* **2016**, *108*, 192405.
- [66] V. Rodionov, A. Amirov, M. Annaorazov, E. Lähderanta, A. Granovsky, A. Aliev, V. Rodionova, *Processes* **2021**, *9*, 772.
- [67] C. P. Bean, D. S. Rodbell, *Phys. Rev.* **1962**, *126*, 104.
- [68] E. Valiev, R. Gimaev, V. Zverev, K. Kamilov, A. Pyatakov, B. Kovalev, A. Tishin, *Intermetallics* **2019**, *108*, 81.
- [69] V. Stanković, C. Comninellis, Rhodium Recovery and Recycling from Spent Materials, **2011**.
- [70] Z. Jia, J. W. Harrell, R. D. K. Misra, *Appl. Phys. Lett.* **2008**, *93*, 022504.
- [71] D. Ciuculescu, C. Amiens, M. Respaud, A. Falqui, P. Lecante, R. E. Benfield, L. Jiang, K. Fauth, B. Chaudret, *Chem. Mater.* **2007**, *19*, 4624.
- [72] D. Ciuculescu, C. Amiens, M. Respaud, P. Lecante, A. Falqui, B. Chaudret, *Mod. Phys. Lett. B* **2007**, *21*, 1153.
- [73] Y. Cao, Y. Yuan, Y. Shang, V. I. Zverev, R. R. Gimaev, R. Barua, R. L. Hadimani, L. Mei, G. Guo, H. Fu, *J. Mater. Sci.* **2020**, *55*, 13363.
- [74] R. Nadarajah, S. Tahir, J. Landers, D. Koch, A. S. Semisalova, J. Wiemeler, A. El-Zoka, S. H. Kim, D. Utzat, R. Möller, B. Gault, H. Wende, M. Farle, B. Gökce, *Nanomaterials* **2020**, *10*, 2362.
- [75] K. J. Merazzo, A. C. Lima, M. Rincón-Iglesias, L. C. Fernandes, N. Pereira, S. Lanceros-Mendez, P. Martins, *Mater. Horiz.* **2021**, *8*, 2654.
- [76] L. Li, B. Post, V. Kunc, A. Elliott, P. Paranthaman, *Scr. Mater.* **2017**, *135*, 100.
- [77] D. Zhang, B. Gökce, S. Barcikowski, *Chem. Rev.* **2017**, *117*, 3990.
- [78] E. Fazio, B. Gökce, A. De Giacomo, M. Meneghetti, G. Compagnini, M. Tommasini, F. Waag, A. Lucotti, C. G. Zanchi, P. M. Ossi, M. Dell'Aglio, L. D'Urso, M. Condorelli, V. Scardaci, F. Biscaglia, L. Litti, M. Gobbo, G. Gallo, M. Santoro, S. Trusso, F. Neri, *Nanomaterials* **2020**, 2317, <https://doi.org/10.3390/nano10112317>.
- [79] B. Gökce, V. Amendola, S. Barcikowski, *ChemPhysChem* **2017**, *18*, 983.
- [80] T. Asahi, F. Mafuné, C. Rehbock, S. Barcikowski, *Appl. Surf. Sci.* **2015**, *348*, 1.
- [81] A. Hahn, T. Stöver, G. Paasche, M. Löbler, K. Sternberg, H. Rohm, S. Barcikowski, *Adv. Eng. Mater.* **2010**, *12*, B156.
- [82] S. Reichenberger, G. Marzun, M. Muhler, S. Barcikowski, *ChemCatChem* **2019**, *11* 4489.
- [83] S. Dittrich, S. Kohsakowski, B. Wittek, C. Hengst, B. Gökce, S. Barcikowski, S. Reichenberger, *Nanomaterials* **2020**, *10*, 1582.
- [84] T. Hupfeld, A. Wegner, M. Blanke, C. Doñate-Buendía, V. Sharov, S. Nieskens, M. Piechotta, M. Giese, S. Barcikowski, B. Gökce, *Adv. Opt. Mater.* **2020**, *8*, 2000473.
- [85] M. B. Wilms, R. Streubel, F. Frömel, A. Weisheit, J. Tenkamp, F. Walther, S. Barcikowski, J. H. Schleifenbaum, B. Gökce, *Procedia CIRP* **2018**, *74*, 196.
- [86] O. Ermak, M. Zenou, G. B. Toker, J. Anki, Y. Shacham-Diamand, Z. Kotler, *Nanotechnology* **2016**, *27* 385201.
- [87] J. Rodríguez-Carvajal, *Phys. B: Condens. Matter* **1993**, *192*, 55.
- [88] J. H. Choi, K. Ryu, K. Park, S.-J. Moon, *Int. J. Heat Mass Transf.* **2015**, *85*, 904.
- [89] A. Kitanovski, *Adv. Energy Mater.* **2020**, *10*, 1903741.
- [90] E. Navarro, M. Multigner, A. R. Yavari, A. Hernando, *EuroPhysLett* **1996**, *35*, 307.
- [91] R. Nadarajah, J. Landers, S. Salamon, D. Koch, S. Tahir, C. Doñate-Buendía, B. Zingsem, R. E. Dunin-Borkowski, W. Donner, M. Farle, H. Wende, B. Gökce, *Sci. Rep.* **2021**, *11*, 17581.
- [92] B. Eggert, A. Schmeink, J. Lill, M. O. Liedke, U. Kentsch, M. Butterling, A. Wagner, S. Pascarelli, K. Potzger, J. Lindner, T. Thomson, J. Fassbender, K. Ollefs, W. Keune, R. Bali, H. Wende, *RSC Adv.* **2020**, *10*, 14386.